ADVANCED OPTICAL MATERIALS
www.advopticalmat.de

Waveguide-Integrated Broadband Spectrometer Based on Tailored Disorder

Wladick Hartmann, Paris Varytis, Helge Gehring, Nicolai Walter, Fabian Beutel, Kurt Busch, and Wolfram Pernice**

Compact, on-chip spectrometers exploiting tailored disorder for broadband light scattering enable high-resolution signal analysis while maintaining a small device footprint. Due to multiple scattering events of light in the disordered medium, the effective path length of the device is significantly enhanced. Here, on-chip spectrometers are realized for visible and near-infrared wavelengths by combining an efficient broadband fiber-to-chip coupling approach with a scattering area in a broadband transparent silicon nitride waveguiding structure. Air holes etched into a structured silicon nitride slab terminated with multiple waveguides enable multipath light scattering in a diffusive regime. Spectral-to-spatial mapping is performed by determining the transmission matrix at the waveguide outputs, which is then used to reconstruct the probe signals. Direct comparison with theoretical analyses shows that such devices can be used for high-resolution spectroscopy from the visible up to the telecom wavelength regime.

1. Introduction

Optical spectroscopy is used in a wide range of applications, e.g., in chemical and biological sensing, material analysis, or light source characterization. To enable low-cost and robust optical spectroscopy for portable sensing or lab-on-a-chip functionality, the development of high-resolution on-chip spectrometers has therefore progressed substantially in recent years. Traditional on-chip spectrometers are often based on Echelle gratings[1–3] and arrayed waveguide gratings,[2,4–7] and require careful design to meet target spectral requirements. The spectral resolution of those devices scales with the optical pathlength, resulting in relatively large footprints (≈1–2 cm^2).

Another promising approach for on-chip broadband spectrometers uses micro-electro-mechanical systems (MEMS) technology combined with Fourier transform infrared spectroscopy.[8–14] These devices are usually fabricated via deep-etching in silicon and are therefore not suitable for applications in the visible wavelength range. A different MEMS-based architecture exploiting propagation of light in air as presented by Mortada et al. allows extending the operation regime to visible wavelengths, yet with moderate resolution at 635 nm wavelength.[9]

As an alternative to wavelength-specific systems, spectrometers based on disordered scattering[15–18] have emerged to enable broadband optical operation. The working principle of such devices is based on the analysis of the speckle pattern which is formed by light after propagation through a disordered medium. The speckle pattern provides a unique "fingerprint," which is usually stored in a beforehand calibrated transmission matrix. As a result, this matrix contains the spectral-to-spatial mapping of the spectrometer. By measuring the "fingerprint," any probe signal can be reconstructed by inverse multiplication with the transmission matrix.

Previous work by Redding et al. demonstrated the possibilities of such a random spectrometer with high resolution and a very compact footprint[19] based on the silicon-on-insulator platform. However, this approach is limited to the telecom wavelength regime due to the transparency window of silicon. For various applications such as Raman spectroscopy[20] or bio-imaging[21] on-chip spectrometers operating both in the near-infrared (NIR) and the visible regime would be desirable. So far, such spectrometers have only been realized, for example, in fiber bundles[17] or single multimode fibers.[18]

In this work, we present an on-chip, compact spectrometer exploiting tailored disorder suitable for a wide wavelength range from the visible to the telecom regime, based on the

W. Hartmann, H. Gehring, N. Walter, F. Beutel, Prof. W. Pernice
Institute of Physics
University of Münster
Wilhelm-Klemm-Str. 10, 48149 Münster, Germany
E-mail: wladick.hartmann@uni-muenster.de;
wolfram.pernice@uni-muenster.de
W. Hartmann, H. Gehring, N. Walter, F. Beutel, Prof. W. Pernice
CeNTech-Center for Nanotechnology
University of Münster
Heisenbergstr.11, 48149 Münster, Germany
P. Varytis, Prof. K. Busch
Theoretical Optics & Photonics
Max-Born-Institut
Max-Born-Str. 2A, 12489 Berlin, Germany
Prof. K. Busch
Institute of Physics
Theoretical Optics & Photonics
Humboldt University Berlin
Newonstr.15, 12489 Berlin, Germany
The ORCID identification number(s) for the author(s) of this article can be found under https://doi.org/10.1002/adom.201901602.

DOI: 10.1002/adom.201901602

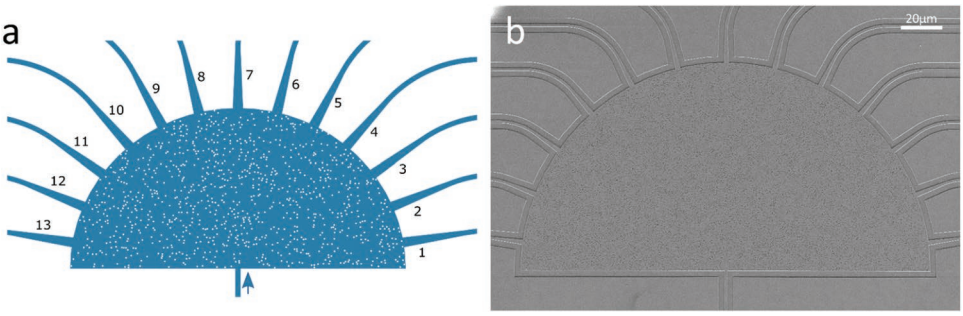

Figure 1. a) Schematic representation of the random scattering spectrometer. Light is launched through the waveguide at the bottom (indicated by the arrow) and detected through the 13 output waveguides which are distributed equally around the scattering area. Due to the semicircle geometry, each output waveguide is located equally distanced from the input waveguide, such that the pathlength of each wavelength is only dependent on the respective mean free path. The numbering of the output waveguides represents also the channel numbers in the transmission matrix shown in Figure 3. b) Scanning electron microscope image of the fabricated device. The random distribution of the scatterers (holes) was calculated using a quantum random number generator.[26] Each hole has a radius of 125 nm, occupying in total 5% of the semicircle area (filling factor). The semicircle has a radius of 100 μm.

silicon nitride platform (Si_3N_4). Not only is silicon nitride suitable for complementary metal-oxide-semiconductor (CMOS) compatible fabrication,[22] but also exhibits a wide transparency window spanning from 300 to 5000 nm and features a relatively large refractive index ($n \approx 2$).[23] To harness the broad operation window offered by both the material platform and the spectroscopy concept, we combine our spectrometer with a 3D polymer based fiber-to-chip coupling technique[24] allowing us to efficiently couple optical bandwidth of more than 1000 nm to our chip. We analyze the performance of our device and provide a comparison with theoretical analyses based on Mie theory.[25]

2. Device Design and Fabrication

Figure 1a depicts the basic design of our device. It is comprised of an input waveguide (bottom) which launches light into a semicircular scattering region with randomly distributed air holes. The distribution of these scatterers is determined using a quantum random number generator[26] in order to maximize true randomness. The filling factor (ff) of the scattering holes determines the total area percentage the holes occupy in the semicircle region. The light then diffuses through the scattering region and is coupled out through 13 output waveguides positioned along the circular edge of the scattering region. Due to the semicircle geometry, the physical distance between input waveguide and each output waveguide is held constant. The width of the waveguides was designed to be 1.3 μm. A linear taper of 2.5 μm is implemented at the outcoupling of the scattering region in order to increase the light collection area. The device itself is fabricated by electron beam lithography utilizing the positive tone resist AR-P 6200 (www.allresist.com) with subsequent reactive ion etching (RIE) into 330 nm thick Si_3N_4 (LPCVD) atop 3.3 μm of buried oxide. Following fabrication of the planar waveguides, the 3D coupling structures are realized by additive manufacturing using direct laser writing (DLW) with a Nanoscribe tool (Nanoscribe Professional GT, 63× objective). A scanning electron microscope (SEM) image of a typical device is depicted in Figure 1b. In order to ensure discrete scattering elements in form of air holes, a design rule of a minimal hole distance of 50 nm is introduced. Nevertheless, due to imperfect fabrication, some holes are fused together, thus creating larger scattering centers, which can influence the diffusive scattering, as can be seen in **Figure 2**d. In Figure 2a, a schematic representation of the whole device is shown. An overview of the fabricated device from a scanning electron microscope image is shown in Figure 2c. In order to provide broadband operation of the device, a novel light-coupling strategy is utilized.[27] In analogy to ref. [24], we employ 3D DLW to realize near-adiabatic polymer fiber-to-waveguide couplers, which offer broadband transmission characteristics. By exploiting total internal reflection (TIR), they provide good mechanical stability while maintaining a bandwidth of over 1000 nm.[24] A close-up image of such a coupling structure is shown in Figure 2b. The 3D couplers exhibit very low insertion losses of around 1.8 dB in the telecom range and an overall coupling efficiency above −8 dB over a broad wavelength range from 730 to 1700 nm. Furthermore, they allow for a relaxed mechanical alignment with respect to optical fibers, with −1 dB alignment tolerance of about 5 μm in the x- and y-directions parallel to the chip surface and −1 dB alignment tolerance in the out-of-plane z-direction of 34 μm. In our recent work on broadband coupling, we also show that the fabrication of many 3D couplers with high yield is highly reproducible.[24,27]

We chose the waveguide geometry to be 1.3 μm in width while the height is 330 nm, determined by the thickness of the waveguiding layer. This geometry is optimized for guiding of TE-polarized light with a suppression of the TM-mode by around 15–20 dB at telecom wavelengths. However, with decreasing wavelengths, both transverse electric (TE) and transverse magnetic (TM) modes are equally supported by the waveguide. Because the 3D couplers are not polarization dependent, both polarizations can therefore be used in our spectrometer device. In order to efficiently couple light in and out of the chip, we use 16 standard SMF-28 fibers in a fiber array configuration with a 127 μm pitch. For ease of alignment, we use two fibers at each edge of the array to couple light in and out of a reference waveguide, therefore leaving only 14 fibers for the device itself (13 output waveguides and 1 input waveguide). Light transmitted through the device is recorded externally using an HP

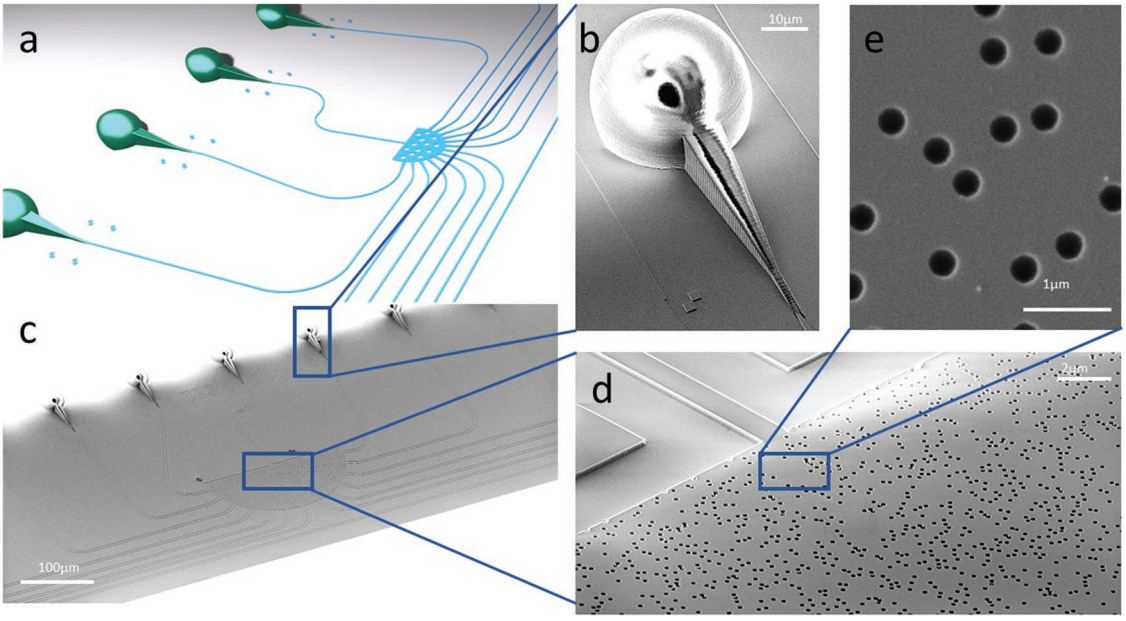

Figure 2. a) 3D schematic representation of the spectroscopic device. Direct laser-written 3D polymer couplers based on total internal reflection (TIR) are used for broadband fiber-to-chip coupling.[24] b) Scanning electron microscope image of one 3D TIR coupler. c) Scanning electron microscope image of the broadband spectrometer device with d) a zoom of the scattering region with multiple air holes as scatterers. Due to fabrication imperfection some holes are fused together despite the design limitation of 50 nm as minimum hole distance. e) A zoom-in view of the etched holes in the scattering region.

8163A power meter with an HP 81634B InGaAs sensor module for infrared measurements and an HP 81530A for visible light measurements.

3. Results

As shown in our previous theoretical work,[25] the resolution of such a spectrometer depends on the light being scattered in a diffusive regime and therefore on the transport mean free path. The resolution improves for shorter wavelengths because also the transport mean free path decreases, respectively. Si_3N_4 was chosen as a waveguiding material because of its large transparency window, making the spectrometer suitable for wavelength ranges from the visible to the near infrared. Due to the smaller refractive index of Si_3N_4 compared to silicon, our device exhibits a slightly larger footprint compared to the structure presented in ref. [19]. Nevertheless, we find that a radius of the scattering region of 100 μm is sufficient for competitive spectrometer operation. Further details regarding the working principle of our spectrometer is described in refs. [19,25]. Since the speckle pattern is recorded after fabrication of the device and then stored in a transmission matrix, which is, in turn, used for the reconstruction of any probe signal, the device is inherently insensitive to any fabrication errors. Any imperfections during fabrication will only influence the speckle pattern itself, but not the spectrometer operation.

To experimentally characterize the optical properties of the fabricated random spectrometers, several tunable laser sources are used for initial calibration (Santec TLS510, Superlum BS930, and NewFocus TLB6700, respectively). The spectrometer is used in transmission mode while sweeping each laser individually, using the power meter to detect the transmitted light. The transmitted intensity of each individual wavelength is recorded for each of the 13 output waveguides and stored in a transmission matrix T (**Figure 3**a,c,e). For the three different wavelength ranges, we chose a 40 nm operation window from 1530 to 1570 nm, a 15 nm window from 950 to 965 nm, and a 15 nm window from 765 to 780 nm, respectively. The bandwidth of these operation windows, and therefore the number of independent spectral channels which can be measured simultaneously, is limited by the number of individual spatial channels. In our setup, the available number of spatial channels is given by the fiber array with 16 fibers, making 13 spatial channels available as described above. The bandwidth is limited to the number of spatial channel times twice the spectral resolution[19] ($2D\delta\lambda$, with D being the number of detectors and $\delta\lambda$ the spectral resolution). Further details can be found in the Supporting Information. The spectral channel spacing for the stored calibration matrix was chosen to be 0.1 nm for each wavelength range, which is less than the respective resolution $\delta\lambda$. In order to determine the resolution of the spectrometer, the spectral correlation function of an individual detector is calculated as[19]

$$C(\Delta\lambda, D_i) = \frac{\langle I(\lambda, D_i)\rangle I\langle\lambda+\Delta\lambda, D_i\rangle}{\langle I(\lambda, D_i\rangle\langle I(\lambda+\Delta\lambda, D_i)\rangle} - 1 \quad (1)$$

where $I(\lambda, D_i)$ denotes the light intensity at wavelength λ and detector D_i ($i = 1, 2, ..., 13$), and the average is taken over the respective wavelength ranges. Finally, the values $C(\Delta\lambda, D_i)$ are subsequently averaged over all 13 detectors and normalized to the value at $\Delta\lambda = 0$ to yield the random spectrometers correlation function $C(\Delta\lambda)$. The dependence of $C(\Delta\lambda)$ on $\Delta\lambda$ is displayed in Figure 3b,d,f. From this graph, the half width at half

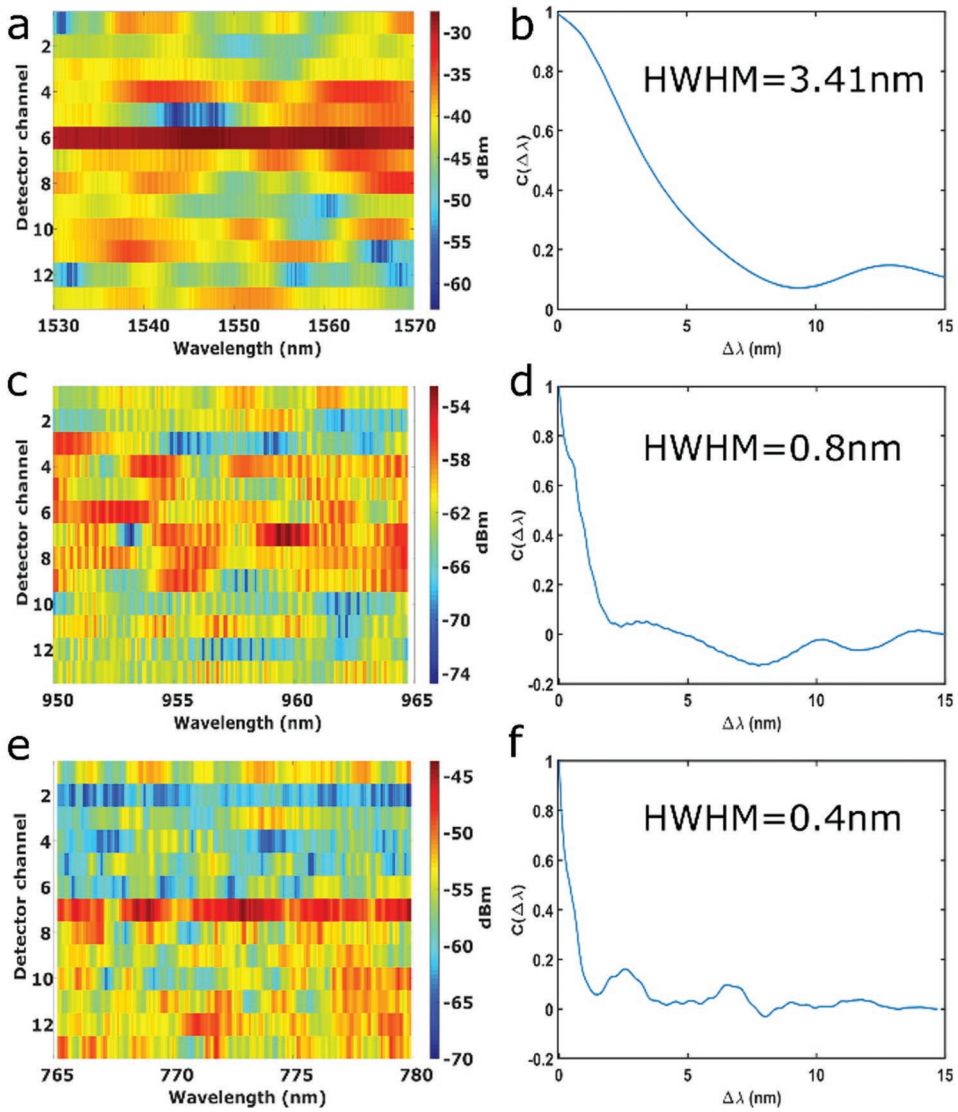

Figure 3. a,c,e) Transmission matrix for near IR light around 1550 and 900 nm and the visible regime around 765 nm, respectively. The detector channel number represents the respective output waveguide number. Each transmission matrix represents the intensity distribution per channel of different wavelengths separated by 0.1 nm. The distribution was measured by sweeping a tunable laser source through the respective wavelength range and measuring the output power of each individual wavelength in each of the 13 output waveguides. b,d,f) Correlation function for each respective wavelength region with the HWHM.

maximum (HWHM) can be directly extracted, providing an estimate of the spectrometers' spectral resolution, $\delta\lambda$, in the respective wavelength ranges.

In ref. [25] we provided a theoretical study of the spectrometer's operation principle at a given geometry for three different wavelength ranges. Here, we perform a quantitative experimental study on the full set of parameters such as the semicircle radius, hole radius, and filling factor of the scatterers. Consequently, we have measured the transmission matrix and calculated the respective correlation function and thus $\delta\lambda$ for a series of parameter sweeps (see the Supporting Information). For rapid prototyping and faster fabrication, we have confined ourselves to only using the near-IR frequency range around 1550 nm where in-plane grating couplers can be used for coupling light from the fiber to the chip. Because of the use of those couplers, light guiding is restricted to TE-polarized light. Using this approach, we have conducted an extensive study of parameter sweeps where we varied the radius of the scattering region from 20 to 140 µm in 20 µm steps, the hole radius from 50 to 200 nm in 20 nm steps, and the filling factor from 5% to 23% in 2% steps. This amounts to a total of 560 characterized devices.

To analyze the performance of the spectrometer not only the HWHM of the correlation function is important, but also the lowest point (minimum) of C. As can be seen, for instance, in Figure 3d, the correlation function drops below zero. The negative value of C can be interpreted as anticorrelation, meaning that for lower values' stronger correlation with a wavelength-dependent intensity distribution exists. Therefore, one has to take into account not only the HWHM but also the minimum of each correlation function. For TE-polarized 1550 nm light,

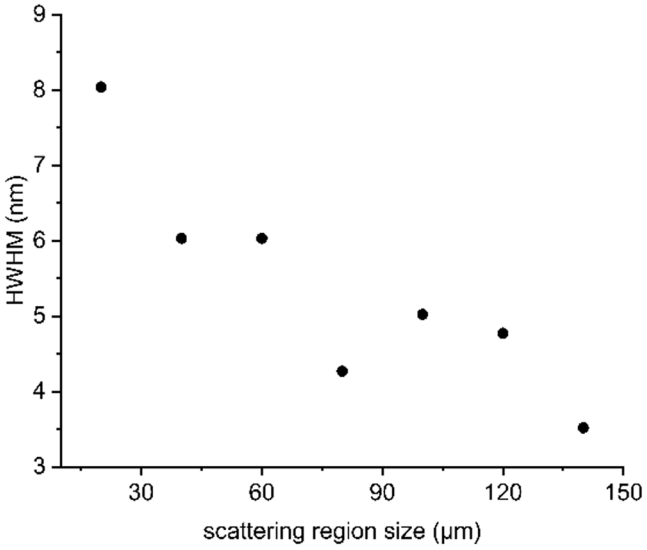

Figure 4. Half width at half maximum of the correlation function for different devices with a fixed radius of the scattering holes of 125 nm and a filling factor of 5% versus the scattering region size (radius of the semicircle).

we found that holes of 125 nm radius covering 5% of the total scattering area provided the best results in terms of these two figures of merit. The HWHM of the correlation function versus the scattering region radius is depicted in **Figure 4**. It is apparent that the HWHM decreases with increasing size of the scattering region, meaning that the resolution of the spectrometer increases. A full plot with all collected data is presented in the Supporting Information.

As stated in ref. [25], the transport mean free path scales with $1/L$ within the diffuse regime, with L being the radius of the scattering region. A short transport mean free path implies strong scattering and is therefore advantageous. The results depicted in Figure 4 experimentally evidence this fact and also illustrate that light scattering in our device takes place in the diffusive regime.

As mentioned above, conventional in-plane grating couplers were used for the parameter sweeps. Because these couplers only support TE-polarized light and a narrow bandwidth of around 100 nm, we fabricated a second chip with the best parameter combinations and used our 3D coupling structure for fiber coupling. For the design of the final device we chose a filling factor of 5% for the scatterers, a scatterer radius of 125 nm, and a radius of the entire device to be 100 μm. In order to avoid that neighboring holes overlap during fabrication and, therefore, would deteriorate the scattering efficiency, a minimal distance in the design has to be introduced. In the parameter sweep of the first chip, this minimal distance was set to 30 nm. As scanning electron microscope images revealed, this distance has been insufficient to completely prevent the fusion of two holes. Therefore, for the devices on a second chip the minimal distance for the final device was set to 50 nm. Figure 2d shows a zoom in SEM image of the final device. Despite the minimal distance of 50 nm, there still are a few holes that lie very close to each other. However, the number of such clustered holes has dramatically reduced compared to the devices with 30 nm minimal hole distance. As a result, by utilizing this adjustment and combining this with the 3D coupler structures, the device shows improved performance in terms of resolution relative to a first-generation device with reduced minimal distance and conventional grating couplers but otherwise identical parameters. A more detailed analysis of this improvement is given further in the "Discussion" section.

Since in integrated optics optical loss is a key figure of merit, we discuss the two major contributions to loss in our final device: fiber-to-chip coupling losses and out-of-plane losses in the scattering region. In refs. [24,27], we have shown that 3D polymer fiber-to-chip couplers can be used for highly broadband and low-loss coupling. Our recent design combines this low-loss functionality with an improved structural stability.

In order to quantify the optical loss by out-of-plane scattering, we sum over the transmission intensities of all 13 output waveguides of our device. By normalizing this value to the intensity measurement of a reference waveguide in close vicinity of the device, we obtain an estimate of the overall transmission of our spectrometer including the out-of-plane loss, but not the fiber-to-chip coupling loss. These estimates are depicted in **Figure 5**a for the infrared range around 1550 nm and in Figure 5b for the visible range. We estimate the mean total loss for the infrared

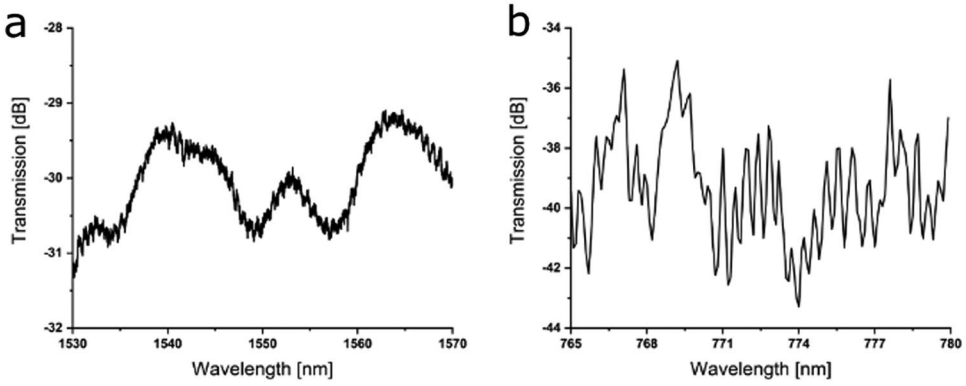

Figure 5. Frequency-resolved measured total transmission into the 13 output ports (including out-couplers) of our random spectrometer for the wavelength range around a) 1550 nm and b) 770 nm. The total transmission is normalized to the transmission of a reference waveguide (including in- and out-couplers) so that the results characterize the actual random spectrometer device including out-of-plane losses. It is clearly visible that the transmission is around 10 dB lower for the visible spectrum as for the infrared. This is due to the much higher scattering efficiency in the visible regime.

regime to be around 30 dB due to out-of-plane scattering while it increases up to a mean value of 39 dB for the visible range. This increase toward higher frequencies and therefore lower wavelengths is to be expected, since also the scattering efficiency increases, as was shown in ref. [25] and out-of-plane scattering becomes stronger. As stated in ref. [19], such scattering loss leads to a decrease in the resolution of the spectrometer because the out-of-plane leakage is larger for light with longer optical paths.

Thereby the effective path length of light reaching the output waveguides and, therefore, the detector is reduced. Since the resolution depends on the optical path length of the scattered light, this directly limits the resolution. Although the loss is significant, this does not directly limit the sensitivity of our device. Because we use low-noise photodetectors with a noise floor of −110 dBm at 1550 nm and −90 dBm at visible wavelengths, our dynamic range of the measurement still remains quite large and, therefore, does not impact the performance of the device. Alternatively, on-chip detectors could be integrated in the future.

In order to use the fabricated device as a spectrometer, first it has to be calibrated. The intensity of light at each output waveguide as a function of wavelength is recorded for wavelength ranges at 765–780, 950–965, and 1530–1570 nm, and stored in a transmission matrix T, respectively (Figure 3a,c,e). The corresponding correlation function with the respective HWHM is shown alongside each transmission matrix. As argued in our theoretical paper,[25] the resolution increases significantly with higher frequencies because of stronger scattering. The measured intensity distribution I is related to the input spectral channels S as $I = TS$. At this point, it is important to note that I and S are vectors of different lengths. More precisely I has 13 elements (i.e., the number of detectors) and the length of S is given by the number of spectral channels corresponding to the respective spectral window (i.e., the wavelength ranges above divided by the aforementioned channel spacing of 0.1 nm) so that the transmission matrix T is far from being quadratic.

After calibration, we reconstruct an arbitrary probe spectrum by measuring its intensity distribution at each output waveguide and using the inverse of T to calculate S by $S = T^{-1} I$. In practice, this approach does not yield satisfying results because the transmission matrix T is not quadratic and thus a pseudoinverse of the matrix must be calculated. Unfortunately, such pseudoinverse matrices are highly susceptible to experimental noise and therefore the reconstruction of a probe spectrum is not feasible.[18,19] Consequently, we employ the method of a truncated inversion technique described in ref. [18]. This inversion approach utilizes a singular value decomposition to factorize the transmission matrix $T = UDV^T$ and employs a truncated version of the singular values D_{trunc}, where elements of the diagonal matrix D that lie below a certain threshold value are set to zero, thus considerably reducing the noise dependence. In order to further improve the accuracy of the reconstructed spectrum, we have combined the truncation process with a nonlinear optimization algorithm to find the unknown spectrum S which minimizes $\|I - TS\|^2$.[18] After optimizing this process, we perform reconstruction of a series of spectral lines across the respective wavelength regimes. The results of this reconstruction are shown in **Figure 6**a,c,e. We further reconstruct two spectral lines in close spectral proximity in order to test the spectrometers' resolution. Since light fields of different frequencies do not interact with each other, we can simply synthesize the probe spectrum by adding the intensities of two spectral lines from two separate laser sources as $I_{\text{probe}} = I_{\lambda,1} + I_{\lambda,2}$. As depicted in Figure 6b,d,f, two spectral lines can be clearly resolved simultaneously. The resolution limit thereby decreases from 3 nm for infrared light to 1 nm at shorter wavelengths and eventually to 0.3 nm for the visible wavelength regime.

4. Discussion

By comparing the device size at a given resolution with our simulations in ref. [25], we note that our experimental device is significantly larger in scattering region size. Although it also exhibits a significantly better resolution compared to the simulation due to longer optical path of the light, we attribute the need for a larger device also to the out-of-plane scattering loss, which was not considered in the 2D simulation of our previous work.

Nevertheless, if we directly compare the results presented here with our theoretical work in terms of the half width at half maximum of the spectral correlation, we find that the device exhibits an improved resolution in the near-infrared decreasing from 5.9 nm for TE- and 4.3 nm for TM-polarized light to 3.4 nm in the experiments. For wavelengths around 900 nm the resolution improves from 1.9 nm (TE) and 2.1 nm (TM) to 1 nm and in the visible regime even from 1 nm for both modes to 0.4 nm.

In addition to limiting the resolution, high transmission loss can prevent the applicability of such a device. Further improvement of the transmission and, therefore, minimization of transmission loss is needed. Such out-of-plane loss can be partially compensated by employing an optical mirror made out of gold or silver on top of the main scattering region, similar to ref. [28]. This can be fabricated by introducing a buffer layer out of SiO_2 of around 1 μm thickness between Si_3N_4 and metal, thus avoiding absorption losses by the metal. Also, by integrating high-efficiency detectors directly on-chip the overall transmission loss of the device could be further decreased.

In addition, the intensity of the out-of-plane scattered light can be further reduced by tailoring the disorder in the system. As Redding et al. show in ref. [19], an improved distribution of the scattering centers can be highly beneficial in order to reduce the out-of-plane scattering significantly while maintaining the resolution of the spectrometer.

Beside the transmission loss we also want to comment on the polarization dependence and performance of our device. As shown in our theoretical work, the scattering efficiency and, therefore, directly the resolution of our spectrometer depend on the light being TE- or TM-polarized, especially for the infrared regime around 1550 nm. Although our final device was designed and fabricated according to the same parameters as the devices of the first generation, whose results are depicted in Figure 4, the measured HWHM of the correlation function differs from 5 to 3.41 nm for a device with 5% filling factor, 125 nm hole radius, and 100 μm scattering region radius. As

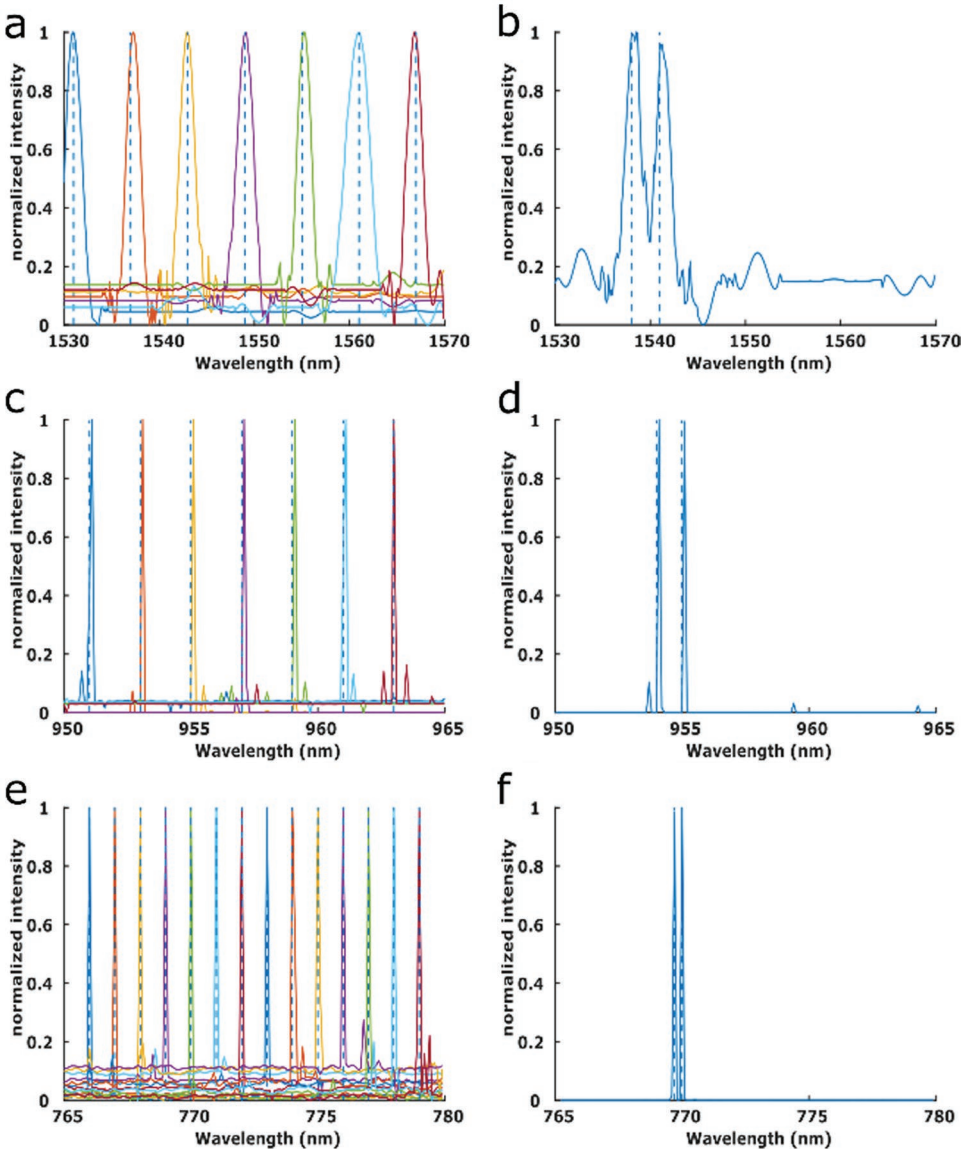

Figure 6. a,c,e) Reconstructed spectra for different narrow spectral lines across the different wavelength regimes. The dotted lines represent the probe signal. The width of the reconstructed lines decreases with decreasing wavelength, verifying the increasing resolution. The separation of the probe signals is 6, 2, and 1 nm, respectively. b,d,f) The reconstruction of two simultaneous probe signals separated by 3, 1, and 0.3 nm, respectively.

mentioned before, we attribute this improvement in resolution partly to the increased minimal distance between holes to 50 instead of 30 nm. But we also would like to mention that with our 3D coupling structures it is possible to couple light of both polarizations into the waveguide as opposed to conventional grating couplers, which are designed for only one specific polarization, in our case the TE mode, inherently losing all the information about the TM mode. Since it is therefore impossible to know which polarization is coupled into the waveguide, we simply use a polarization controller to optimize the transmission through a reference waveguide without any scattering region and keep all fibers fixed during the experiment. However, since the input fiber to the device is a different fiber than used for the reference waveguide, due to the usage of a fiber array, the polarization launched into the device is not necessarily the same as the one launched into the reference waveguide. Consequently, we assume that the actual polarization inside the waveguides and thus also inside the scattering region is a mixed mode comprised of TE- and TM-polarized light.

Therefore, we attribute the increase in resolution to both the increased minimal distance and the change in polarization in our final device, which is only possible with polarization-independent couplers.

5. Conclusion

We have realized a broadband and compact on-chip spectrometer based on random scattering. Our experimental results are in good agreement with theoretical findings over several

parameter ranges that we have considered experimentally. We have obtained transmission matrices for three different wavelength regimes ranging from visible to telecom wavelengths. With broadband fiber-to-chip couplers, we obtain bandwidth of almost 1000 nm as demonstrated by the successful reconstruction of several probe signals separately and also simultaneously. Because of the operation principle based on spectral-to-spatial mapping, the same random spectrometer can be used for all wavelengths. Only the calibration matrix has to be recorded once for the desired wavelength range and stored. Further improvement in sensitivity and resolution can be achieved co-integrating the random spectrometer together with on-chip detectors.[29] Furthermore, the integration of on-chip detectors makes it possible to significantly increase the number of output ports, thus increasing the resolution.

Supporting Information

Supporting Information is available from the Wiley Online Library or from the author.

Acknowledgements

The authors acknowledge support by the Deutsche Forschungsgemeinschaft (DFG) within the priority program DFG-SPP 1839 "Tailored Disorder," projects Bu 1107/10-1, BU 1107/10-2, PE 1832/5-1, and PE 1832/5-2.

Conflict of Interest

The authors declare no conflict of interest.

Keywords

broadband light scattering, infrared light, integrated optics, random spectrometers, silicon nitride, tailored disorder, visible spectrum

Received: September 23, 2019
Revised: November 18, 2019
Published online: January 22, 2020

[1] S. Janz, A. Balakrishnan, S. Charbonneau, P. Cheben, M. Cloutier, A. Delage, K. Dossou, L. Erickson, M. Gao, P. A. Krug, B. Lamontagne, M. Packirisamy, M. Pearson, D. Xu, *IEEE Photonics Technol. Lett.* **2004**, *16*, 503.
[2] J.-J. He, B. Lamontagne, A. Delage, L. Erickson, M. Davies, E. S. Koteles, *J. Lightwave Technol.* **1998**, *16*, 631.
[3] R. Cheng, C.-L. Zou, X. Guo, S. Wang, X. Han, H. X. Tang, *Nat. Commun.* **2019**, *10*, 1.
[4] P. Cheben, J. H. Schmid, A. Delâge, A. Densmore, S. Janz, B. Lamontagne, J. Lapointe, E. Post, P. Waldron, D.-X. Xu, *Opt. Express* **2007**, *15*, 2299.
[5] T. Fukazawa, F. Ohno, T. Baba, *Jpn. J. Appl. Phys.* **2004**, *43*, L673.
[6] K. Okamoto, K. Moriwaki, S. Suzuki, *Electron. Lett.* **1995**, *31*, 184.
[7] M. Zirngibl, C. Dragone, C. H. Joyner, *IEEE Photonics Technol. Lett.* **1992**, *4*, 1250.
[8] L. P. Schuler, J. S. Milne, J. M. Dell, L. Faraone, *J. Phys. D: Appl. Phys.* **2009**, *42*, 133001.
[9] B. Mortada, M. Erfan, M. Medhat, Y. M. Sabry, B. Saadany, D. Khalil, *J. Lightwave Technol.* **2016**, *34*, 2145.
[10] N. P. Ayerden, U. Aygun, S. T. S. Holmstrom, S. Olcer, B. Can, J.-L. Stehle, H. Urey, *Appl. Opt.* **2014**, *53*, 7267.
[11] Y. M. Eltagoury, Y. M. Sabry, D. A. Khalil, *Proc. SPIE* **2016**, *9760*, 97600L.
[12] D. Khalil, Y. Sabry, H. Omran, M. Medhat, A. Hafez, B. Saadany, *Proc. SPIE* **2011**, *7930*, 79300J.
[13] Y. M. Eltagoury, Y. M. Sabry, D. A. Khalil, *Adv. Mater. Technol.* **2019**, *4*, 1900441.
[14] A. O. Ghoname, Y. M. Sabry, M. Anwar, A. Saeed, B. Saadany, D. Khalil, *Proc. SPIE* **2019**, *10931*, 109310Z.
[15] Z. Xu, Z. Wang, M. E. Sullivan, D. J. Brady, S. H. Foulger, A. Adibi, *Opt. Express* **2003**, *11*, 2126.
[16] T. W. Kohlgraf-Owens, A. Dogariu, *Opt. Lett.* **2010**, *35*, 2236.
[17] Q. Hang, B. Ung, I. Syed, N. Guo, M. Skorobogatiy, *Appl. Opt.* **2010**, *49*, 4791.
[18] B. Redding, S. M. Popoff, H. Cao, *Opt. Express* **2013**, *21*, 6584.
[19] B. Redding, S. F. Liew, R. Sarma, H. Cao, *Nat. Photonics* **2013**, *7*, 746.
[20] A. Dhakal, F. Peyskens, S. Clemmen, A. Raza, P. Wuytens, H. Zhao, N. Le Thomas, R. Baets, *Interface Focus* **2016**, *6*, 20160015.
[21] S. K. Gayen, R. R. Alfano, *Opt. Photonics News* **1996**, *7*, 16.
[22] D. J. Moss, R. Morandotti, A. L. Gaeta, M. Lipson, *Nat. Photonics* **2013**, *7*, 597.
[23] S. V. Deshpande, E. Gulari, S. W. Brown, S. C. Rand, *J. Appl. Phys.* **1995**, *77*, 6534.
[24] H. Gehring, M. Blaicher, W. Hartmann, P. Varytis, K. Busch, M. Wegener, W. H. P. Pernice, *APL Photonics* **2019**, *4*, 010801.
[25] P. Varytis, D.-N. Huynh, W. Hartmann, W. Pernice, K. Busch, *Opt. Lett.* **2018**, *43*, 3180.
[26] https://qrng.physik.hu-berlin.de/, **2019**.
[27] H. Gehring, A. Eich, C. Schuck, W. H. P. Pernice, *Opt. Lett.* **2019**, *44*, 5089.
[28] W. S. Zaoui, M. F. Rosa, W. Vogel, M. Berroth, J. Butschke, F. Letzkus, *Opt. Express* **2012**, *20*, B238.
[29] S. Ferrari, O. Kahl, V. Kovalyuk, G. N. Goltsman, A. Korneev, W. H. P. Pernice, *Appl. Phys. Lett.* **2015**, *106*, 151101.